Nano-Micro Letters

e-ISSN 2150-5551
CN 31-2103/TB

ARTICLE

https://doi.org/10.1007/s40820-025-01858-2

Cite as
Nano-Micro Lett.
(2026) 18:15

Received: 29 April 2025
Accepted: 30 June 2025

Quantum-Size FeS_2 with Delocalized Electronic Regions Enable High-Performance Sodium-Ion Batteries Across Wide Temperatures

Tianlin Li[1], Danyang Zhao[1,2] ✉, Meiyu Shi[1], Chao Tian[1], Jie Yi[1], Qing Yin[1,2], Yongzhi Li[1,2], Bin Xiao[1,2], Jiqiu Qi[1,2], Peng Cao[3], Yanwei Sui[1,2] ✉

HIGHLIGHTS

- Quantum-scaled FeS_2 induces delocalized electronic regions, effectively reducing electrostatic potential barriers and accelerating Na^+ diffusion kinetics.
- The free charge accumulation regions were formed by edge mismatched atoms, activating numerous electrochemically sites to enable high-capacity Na^+ storage and ultrafast-ion transport across wide temperature range (−35 to 65 °C).
- The FeS_2 QD/MXene anode delivers superior wide-temperature capacity of 255.2 mAh g^{-1} (−35 °C) and 424.9 mAh g^{-1} (65 °C) at 0.1 A g^{-1}. The FeS_2 QD/MXene//NVP cell achieves a record energy density of 162.4 Wh kg^{-1} at − 35 °C.

ABSTRACT Wide-temperature applications of sodium-ion batteries (SIBs) are severely limited by the sluggish ion insertion/diffusion kinetics of conversion-type anodes. Quantum-sized transition metal dichalcogenides possess unique advantages of charge delocalization and enrich uncoordinated electrons and short-range transfer kinetics, which are crucial to achieve rapid low-temperature charge transfer and high-temperature interface stability. Herein, a quantum-scale FeS_2 loaded on three-dimensional Ti_3C_2 MXene skeletons (FeS_2 QD/MXene) fabricated as SIBs anode, demonstrating impressive performance under wide-temperature conditions (− 35 to 65 °C). The theoretical calculations combined with experimental characterization interprets that the unsaturated coordination edges of FeS_2 QD can induce delocalized electronic regions, which reduces electrostatic potential and significantly facilitates efficient Na^+ diffusion across a broad temperature range. Moreover, the Ti_3C_2 skeleton reinforces structural integrity via Fe–O–Ti bonding, while enabling excellent dispersion of FeS_2 QD. As expected, FeS_2 QD/MXene anode harvests capacities of 255.2 and 424.9 mAh g^{-1} at 0.1 A g^{-1} under − 35 and 65 °C, and the energy density of FeS_2 QD/MXene//NVP full cell can reach to 162.4 Wh kg^{-1} at − 35 °C, highlighting its practical potential for wide-temperatures conditions. This work extends the uncoordinated regions induced by quantum-size effects for exceptional Na^+ ion storage and diffusion performance at wide-temperatures environment.

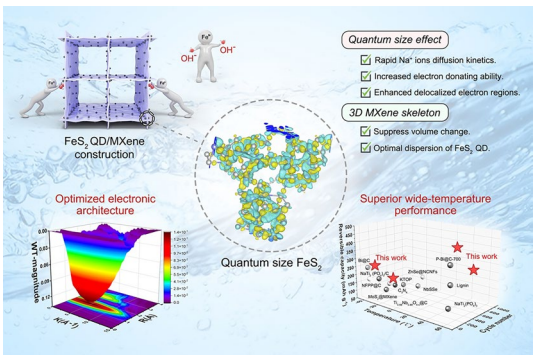

KEYWORDS Quantum-size effect; Electron delocalization; Efficient short-range transfer kinetics; Wide-temperature; Sodium-ion batteries

✉ Danyang Zhao, zhao_dy@cumt.edu.cn; Yanwei Sui, wyds123456@outlook.com
[1] China University of Mining and Technology, Xuzhou 221116, People's Republic of China
[2] Jiangsu Province Engineering Laboratory of High-Efficient Energy Storage Technology and Equipment, School of Materials Science and Physics, China University of Mining and Technology, Xuzhou 221116, People's Republic of China
[3] Department of Chemical and Materials Engineering, University of Auckland, Auckland 1142, New Zealand

Published online: 29 July 2025

Shanghai Jiao Tong University Press

Springer

1 Introduction

Sodium-ion batteries (SIBs) have emerged as a significant technological innovation, due to the abundance of sodium resources, superior safety features and lower cost, which can be promising alternative for lithium-ion batteries devices ascribing to their similar redox mechanisms [1, 2]. Although SIBs have exhibit dramatically improved electrochemical performance in recent years, the wide-temperature (− 35 to 65 °C) properties have also been the crucial bottleneck for expanding the application of SIBs, which are mainly hindered by poor ion conduction efficiency and reduced diffusion kinetics of electrodes [3–6]. Therefore, developing novel anodes with high capacity, long lifespan and fast-ion transport is essential to address bottlenecks in the development of wide-temperature SIBs [7].

Ferrous disulfide (FeS_2), a prominent transition metal dichalcogenides (TMDs), demonstrates the sodium storage ability, coupling conversion and alloying mechanisms ($FeS_2 + 4Na^+ + 4e^- \leftrightarrow Fe + 2Na_2S$) [8–10]. Furthermore, FeS_2 is considered as a potential anode material due to abundant reserves, low cost and remarkable theoretical capacity (894 mAh g^{-1}) [11, 12]. However, FeS_2 electrodes typically exhibit sluggish Na^+ diffusion barriers, poor reversibility and substantial volume changes during operation [13]. At low temperature (below − 25 °C), increased electrolyte viscosity impedes ion and charge transfer, resulting in slow reaction kinetics. In contrast, high-temperature (above 50 °C) condition enhances system energy, leading to more active interfacial side reactions and consequently resulting in severe capacity [14, 15].

Various strategies have been proposed to address these challenges including size regulation, defect fabrication and electronic optimization [16–20]. For instance, constructing the defective regions directionally (vacancies, doping, grain boundaries, etc.) can effectively regulate the electrochemical active sites at the atomic level, thereby enhancing Na^+ storage capacity and conversion kinetics. Cao et al. demonstrated that confining SnS within N/S co-doped graphene could reduce the energy activation and enhance power density [16]. However, although N/S-doped carbon has shown improved electronic conductivity and increased active sites, undesirable defect concentrations and incomplete utilization of active materials still restrain the electrochemical performance to a high level. The direct introduction of defect states into active components is considered as a potential avenue to improve its defect concentration. Our group developed a porous conducting matrix confining defect-rich $CoSe_{0.5}S_{1.5}$ composite, the defect manufacturing strategy effectively optimizes charge distribution and electrochemical activity, the prepared $CoSe_{0.5}S_{1.5}$/GA anode could possess superior rate performance 288.2 mAh g^{-1} at 5 A g^{-1}-based sodium-ion capacitor [17]. However, such defect engineering strategies primarily rely on chemical doping or vacancy creation, which inevitably compromise structural stability and limit accessible defect density. This intrinsic trade-off between defect concentration and stability poses a fundamental challenge for achieving wide-temperature adaptability. Therefore, wide-temperature (− 35 to 65 °C) electrode still remains a key issue.

Recent studies have established that edged uncoordinated atoms could effectively promote local electron delocalization, enhance interfacial charge interactions and improve the conversion reaction reversibility [18, 19]. Notably, quantum-size effects naturally maximize the proportion of edge uncoordinated atoms without relying on extrinsic defect engineering. Compared to conventional defect regulation, quantum confinement intrinsically amplifies charge delocalization through unsaturated coordination edges while maintaining structural robustness, a critical advantage for wide-temperature operation. In conclusion, we proposed an innovative strategy for constructing quantum-sized TMDs to maximize the edge atomic content. Nevertheless, TMDs with quantum sizes ranging from 5 to 10 nm tend to agglomerate during the ion insertion and diffusion process due to their high activity; hence, it is crucial to employ an appropriate carrier, which can achieve optimized dispersion and construct strong interfacial coupling of TMDs component. Carbonaceous materials such as activated carbon and graphene have captured extensive attention to serve as substrates to buffer volume change [20–22]. For instance, Zhou and colleagues developed a SIBs anode using SnS/SNC, and the SNC matrix not only achieves uniform dispersion of SnS but also effectively enhances the electrode stability during the electrochemical reaction process [22]. However, traditional carbon materials exhibit unsatisfactory capability in Na^+ energy storage systems due to their inherent electrochemical reaction mechanisms.

Consequently, we have explored two-dimensional transition metal carbides and carbonitrides (MXene) as substrate, which can possess a graphene-like structure and deliver

 https://doi.org/10.1007/s40820-025-01858-2

higher specific capacity. Ti_3C_2 MXene has garnered significant interest due to its excellent metal-level carrier transport efficiency and abundance of surface oxygen-containing functional groups, showing promising potential in the field of energy storage and catalysis applications [23, 24]. Furthermore, recent studies have demonstrated that Ti_3C_2 MXene can be gelatinization by divalent metal ions and form a three-dimensional porous skeleton, which enrich the active sites and restrict the self-stacking effect [25]. This robust 3D network is fabricated via the strong interaction between multivalent metal ions and MXene surface terminations and effectively alleviates the structure collapse, associated with TMD-based electrodes.

Herein, a hybrid of well-dispersed and uniform-loading FeS_2 quantum dot embedded in three-dimensional Ti_3C_2 MXene skeleton (FeS_2 QD/MXene) is fabricated. Compared with conventional well-crystallized TMDs materials, the existence of quantum-scale FeS_2 could manipulate uncoordinated electronic states, supply ample reaction active sites and accelerate the charge transfer kinetic, which contributes to high-efficiency sodium storage under wide temperature. Density functional theory (DFT) calculations and X-ray absorption spectroscopy (XAS) analyses demonstrate that the FeS_2 QD plays a crucial role in expanding charge delocalization regions, enhancing negative electrostatic potential and accelerating ions transport. Importantly, the robust interfacial coupling between FeS_2 QD and MXene substrates could be beneficial to structural stability and electrolyte transportation process. Benefiting from these features, the prepared anode exhibited excellent temperature tolerance (255.2 and 424.9 mAh g^{-1} at 0.1 A g^{-1} under − 35 and 65 °C) and remarkable cycling stability (370.1 mAh g^{-1} at 1 A g^{-1} after 2500 cycles). In addition, the assembled FeS_2 QD/MXene//NVP full cell presents a high energy density of 162.4 Wh kg^{-1} at 0.1C under − 35 °C. This quantum-scale-induced electronic property modulation strategy provides a new path for developing long-life and high-capacity SIBs anodes operated under wide-temperature conditions.

2 Experimental Section

2.1 Materials

Ferrous chloride ($FeCl_2$), Ti_3AlC_2 powder, lithium fluoride (LiF), hydrochloric acid (HCl, 12 M), thioacetamide (TAA), vanadium phosphate sodium ($Na_3V_2(PO_4)_3$), ac ethylene black, polyvinylidene difluoride (PVDF), *N*-methylpyrrolidone (NMP), ethanol (AR, 99.5%) are ordered from Aladdin Reagents (Shanghai) Co., Ltd. All chemicals are used directly without any further treatment.

2.2 Preparation of MXene Suspension

One gram of Ti_3AlC_2 powder was mixed with 1 g LiF and 20 mL 12 M HCl and stirred at 35 °C for 24 h. The mixture was washed by centrifugation at 3500 r min^{-1} several times until the pH of the supernatant turned to 6 ~ 7. MXene precipitate was collected and mixed with 50 mL of deionized water. Ultrasonic treatment of the mixture was performed under argon for 6 h. A single-layer MXene suspension was then obtained by centrifugation at 3500 r min^{-1} for 1 h.

2.3 Synthesis of FeS_2 QD/MXene and Fe^{2+}/MXene

The 2 mL of $FeCl_2$ solution (1 M) was added into 20 mL MXene suspension. After standing for 10 min, Fe^{2+} induced MXene nanosheets to form a three-dimensional network structure. After freeze-drying for 48 h, the 3D MXene-loaded Fe^{2+} composite (Fe^{2+}/MXene) was obtained, and the mass ratio of Fe^{2+}/MXene is ~ 1.12:1. Then, the TAA and prepared composite with a mass ratio of 5:1 are, respectively, placed into two quartz boats; the Fe^{2+}/MXene powders are vulcanized at 300 °C for 2 h in pure Ar_2 atmosphere (2 °C min^{-1}). After naturally cooling down to room temperature, the FeS_2 QD/MXene is achieved.

In addition, the quantum dot structures with other metal ions were realized by same operation (adding 2 mL MCl_2 solution, M = Co^{2+}, Ni^{2+} into 20 mL MXene suspension).

2.4 Synthesis of FeS_2 /MXene

MXene suspension (40 mL) was put into a Teflon liner (80 mL) followed by a certain amount of $FeCl_2$ solution. After stirring for 30 min, the mixed solution was treated by hydrothermal reaction in a stainless-steel reaction still under 150 °C for 10 h. And the cooled reaction mixture was centrifuged 3–5 times with deionized water and dried by freeze-drying to obtain FeS_2/MXene.

3 Results and Discussion

3.1 Design Principle and Structural Characterizations

Theoretical calculations were conducted to predict the effects of size variations on the local electronic coordination environment and charge transport efficiency of the FeS_2 structure before the experimental investigation (Fig. 1a, b). The difference charge density (DCD) of FeS_2 and FeS_2 QD was calculated based on the prior theoretical assumptions (Fig. 1b), and the depletion regions and charge accumulation were, respectively, depicted in blue and red. Obviously, electron rearrangement could be observed at the crystal boundaries and edges of the FeS_2 QD structure, which means that abundant unpaired S atoms serve as negative charge centers, facilitating the bonding of metal atoms. Moreover, to assess their sodium storage capacities, we have identified five possible adsorption sites for Na atom on both FeS_2 and FeS_2 QD models and calculated the Na adsorption energy using Eq. S1 to assess their sodium storage capacities. As shown in Fig. S1, the weakest adsorption occurs when the Na atom is located above the Na–S bond (site 4); the phenomenon consistently could be similarly observed in the FeS_2 QD structure (site 5). This can be attributed to the stable Fe–S bonding, where the saturation of surrounding electrons diminishes the capability to bind Na atoms. The vacancy region (site 5) was the most favorable adsorption site, exhibiting the highest adsorption energy (− 2.25 eV), which contributed to the elevated electron density at the vacancy, and facilitate the formation of Na–S bonds. Obviously, the restricted electronic activity of bulk FeS_2 elevates kinetic barriers for initial Na^+ insertion, resulting in insufficient capture and accommodation of Na^+ during the conversion reaction [26]. This is exacerbated by the structural integrity of basal planes, which anchors electrons in symmetric orbitals, limiting active sites for Na^+ adsorption. Meanwhile, lower electronic conductivity induces severe voltage polarization during cycling, reducing accessible sodium ions and degrading capacity [27]. Consequently, the construction of quantum dot structures played a crucial role in disrupting the coordination integrity of basal planes and forming additional edge free electrons, thus enhancing electrochemical activity. The edge positions in FeS_2 QD enriched with defects became new preferential adsorption sites (site 1–3), where the calculated adsorption energies reach − 3.73, − 3.92, and − 3.85 eV, significantly exceeding those observed in FeS_2. The foreign Na^+ could preferentially bond with the unsaturated edge S atoms of the edge defect, establishing a strengthened interatomic interaction, and demonstrating a stronger chemical affinity and higher adsorption energy on FeS_2 QD. The above calculation results highlight the fast-ion diffusion and storage capabilities due to the delocalized electronic engineering induced by quantum dot structure, which are expected to deliver excellent wide-temperature performance. The DFT calculations provided critical guidance for the structural design. Specifically, theoretical predictions revealed that FeS_2 QD exhibit enhanced charge delocalization at edges due to unsaturated sulfur coordination, which directly motivated our strategic focus on synthesizing quantum-sized FeS_2 to harness these advantages. Consequently, the synthesis strategy of confining FeS_2 on 3D MXene framework was to stabilize QD. As illustrated in Fig. 1a, the controllable preparation of FeS_2 QD/MXene composite was obtained. The Ti_3C_2 MXene was first obtained by a LiF/HCl etching method, followed by Fe^{2+}-induced self-assembly where MXene nanosheets were interconnected through Fe^{2+} ions to construct an interlinked 3D porous substrate, providing an optimal skeleton for FeS_2 QD anchoring.

A detailed morphology evolution of FeS_2 QD/MXene was characterized using scanning electron microscope (SEM) and transmission electron microscope (TEM). As displayed in Fig. S2a, the MXene substrate possesses a two-dimensional morphology, but the inherent self-restacking could reduce the electrochemically active surface area and prevent Na^+ diffusion. The Fe^{2+} ion-induced method could overcome the electrostatic repulsion between the MXene nanosheets and connect them to construct a 3D MXene skeleton (Fig. S2), which suppresses the self-stacking phenomenon and improves the interfacial utilization. The strong interaction between Fe^{2+} and Ti_3C_2 surface could guarantee the uniformity distribution of Fe^{2+} species during the subsequent sulfuration treatment, which can inhibit the agglomeration of highly active FeS_2 QD. The nitrogen adsorption–desorption isotherm curves in Fig. S3 further verified the effective synthesis of porous structures. Distinct from MXene (13.9 $m^2\ g^{-1}$) and FeS_2/MXene (14.4 $m^2\ g^{-1}$), the Fe^{2+}/MXene and FeS_2 QD/MXene, respectively, showed a higher specific surface area (SSA) of 24.7 and 27.2 $m^2\ g^{-1}$, which are contributed to the mesopores indicated by the type IV adsorption isotherm [28, 29]. Pore

https://doi.org/10.1007/s40820-025-01858-2

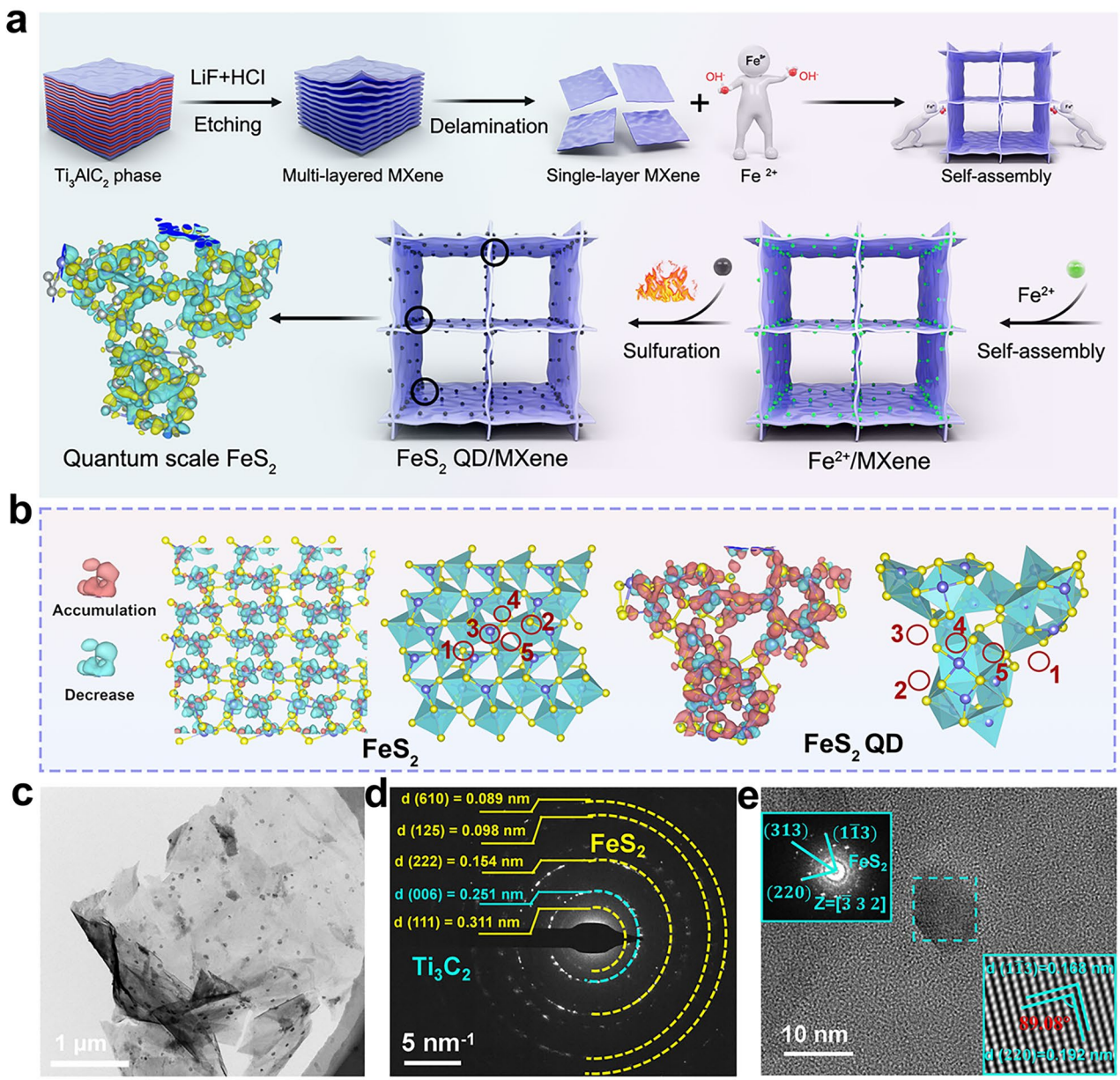

Fig. 1 **a** Schematic illustration of synthesis process about FeS_2 QD/MXene. **b** Schematic representation of the optimization mechanism of the quantum-size effect. **c** TEM image, **d** SAED pattern, **e** HRTEM image of FeS_2 QD/MXene

size distribution diagram exhibited that the average pore size distribution of FeS_2 QD/MXene composite is concentrated in 2–6 nm, showing a typical mesoporous feature. The obvious hysteresis ring in curves also proved the existence of mesoporous structures [30]. The increased SSA and porous structure could provide additional transport channels, which can not only facilitate electrolyte infiltration during cycling but also alleviate the volume changes.

TEM images of FeS_2 QD/MXene described that FeS_2 QD existed with a diameter of 5–8 nm homogeneously dispersed on the MXene surface (Figs. 1c and S4), which maintain uniform dispersion characteristics. In Fig. 1d, the selected area electron diffraction (SAED) pattern image clearly exhibited diffraction rings assigned to the Ti_3C_2 and FeS_2, which, respectively, coincide with the (006) crystal plane of Ti_3C_2 and the (111), (222), (125), and (610) planes of

FeS_2 [31, 32]. The clear lattice shown in Fig. 1e indicated good crystallinity of FeS_2 QD, and the distance of 0.168 nm and 0.192 nm could, respectively, be ascribed to ($\bar{1}$ 13) and (220) lattice plane. In addition, the high-angle annular dark-field (HAADF) image and elemental mapping analysis of FeS_2 QD/MXene composite could confirm the presence and homogeneous distribution of Fe, S, Ti, C, and O species, certifying the uniform dispersion of the FeS_2 particle on the Ti_3C_2 MXene (Fig. S5). Moreover, the thermogravimetric analysis (TGA) was applied to estimate the weight ratio of FeS_2 in FeS_2 QD/MXene, and the calculated ratio was around 36.6% (Fig. S6).

3.2 Interaction Characterization and Mechanical Properties

X-ray diffraction (XRD) patterns are shown in Fig. 2a; the broadened (002) peak could be observed in MXene, FeS_2/MXene, Fe^{2+}/MXene and FeS_2 QD/MXene composites attributing to Ti_3C_2 substrate. In addition, the (002) peak of Fe^{2+}/MXene and FeS_2 QD/MXene shifted to the lower angel, which proves that metal ion gelation method effectively promotes the expansion of layer spacing and the construction of three-dimensional structures [28]. Diffraction peaks of FeS_2 QD/MXene match well with planes of FeS_2 (JPDS No. 97-5-3529) in FeS_2/MXene composite with slightly reduced intensity, which might be attributed to the defect-rich structure. Raman spectra were analyzed to identify chemical bonding states and molecular structures evolution (Figs. 2b and S7). Peaks located at around 271 cm^{-1} were attributed to the Fe–S bands of FeS_2 in FeS_2 QD/MXene and FeS_2/MXene, while the peaks located at around 420 and 620 cm^{-1} are, respectively, corresponding to the vibrations of Ti–C bonds of Mxene [33, 34]. And the bands between 1250 and 1750 cm^{-1} were, respectively, corresponding to the D-band and G-band of Ti_3C_2 Mxene [35, 36]. It is obvious that peaks belonging to Ti–C and Fe–S bonds in the FeS_2 QD/MXene composite shifted toward the low wavenumbers than that of FeS_2/MXene. This phenomenon could be attributed to the formation of Ti–O–Fe bonds located at 190 cm^{-1}, the presence of which inevitably promotes charge rearrangement around the active sites, resulting in electron density decreasing near the Fe–S and Ti–C bonds, and causing a redshift of the corresponding peaks [37]. In addition, the Ti–O–Fe peaks of FeS_2 QD/MXene showed relatively higher strengths compared with Fe^{2+}/MXene and FeS_2/MXene counterparts, indicating the excellent interfacial coupling. A series of analyses of chemically bonded coordination environments and states proved that quantum-sized FeS_2 triggered charge distribution change and electron diffusion, which could be beneficial for the ion storage performance.

X-ray photoelectron spectroscopy (XPS) measurements were taken to analyze the electronic structure of prepared materials. The spectra, respectively, attributed to the Ti–C $2p_{3/2}$, Ti–C $2p_{1/2}$, Ti(II) $2p_{3/2}$, Ti(II) $2p_{1/2}$, Ti(IV) $2p_{3/2}$ and Ti(IV) $2p_{1/2}$, depicted in Fig. S8a [38]. The Ti $2p$ peak positions of FeS_2 QD/MXene showed a positive shift compared to FeS_2/MXene, indicating a decrease in the electron density. As for the Fe elements (Fig. 2c), it could be deconvoluted into eight peaks, respectively, assigned to Fe(II) $2p_{3/2}$, Fe(II) $2p_{1/2}$, Fe(III) $2p_{3/2}$ and Fe(III) $2p_{1/2}$ [39, 40]. Notably, the Fe $2p$ and S $2p$ peaks of the FeS_2 QD/MXene and Fe^{2+}/MXene samples were shifted toward higher binding energies compared to these of FeS_2/MXene, indicating that the electronic structure is obviously different from that of FeS_2/MXene due to the abundant defects. The coordination environment and bonding state proved that the quantum size triggered charge delocalization, thus maximizing the concentration of uncoordinated electrons at FeS_2 edge, which could optimize the sodium storage and transport ability. As depicted in Fig. 2d, the electron paramagnetic resonance (EPR) measurements illustrated that charge rearrangement could produce abundant structural defects. The presence of unpaired electrons caused four samples to exhibit a symmetric Lorentzian line with a g value of around 2.003 [41]. Moreover, the FeS_2 QD/MXene composite possessed the highest vibration intensity, indicating that the largest defect concentration generated in crystal structure. The phenomenon revealed that highly dispersed FeS_2 QDs could deliver a mass of free unpaired electrons, which could regulate the charge distribution and optimize the phase disorder and further increase the Na^+ ions storage sites exposure and shorten ion-transfer distance to achieve significant wide-temperature reversible capacity.

To accurately analyze the local coordination environment of Fe atoms, X-ray absorption spectroscopy (XAS) was performed. The Fe K-edge XAFS (Fig. 2e) showed that the Fe absorption edge for FeS_2 QD/MXene shifts toward higher energy than that of FeS_2 QD/MXene, further indicating the more positively charged state of central Fe atoms, which is consistent with XPS results. It demonstrated that efficient electron transfers from Ti_3C_2 interface to FeS_2 QD, leading

 https://doi.org/10.1007/s40820-025-01858-2

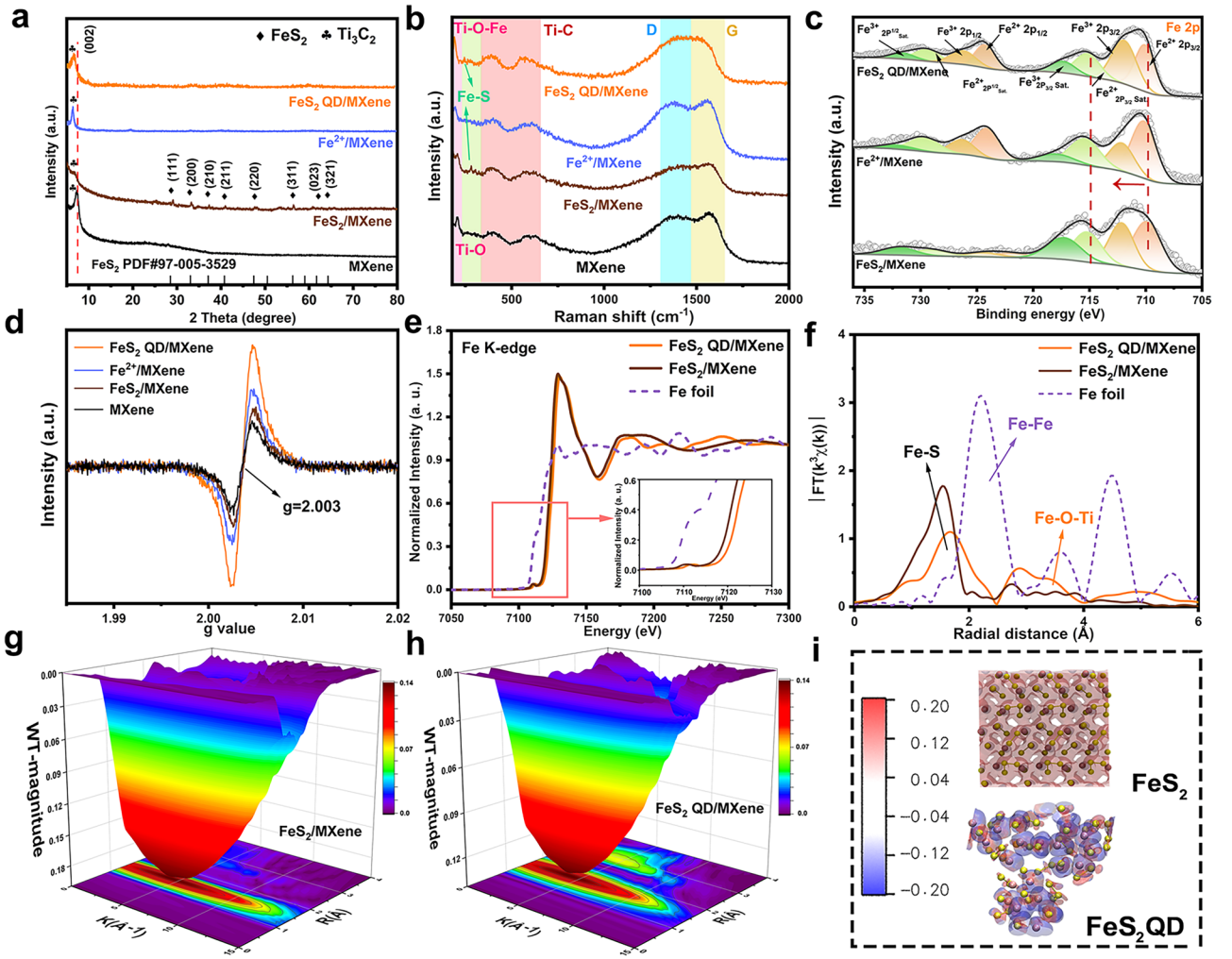

Fig. 2 **a** XRD patterns and **b** Raman spectra, **c** high-resolution XPS spectra of Fe 2*p* and **d** electron paramagnetic resonance images of MXene, FeS_2/MXene, Fe^{2+}/MXene and FeS_2 QD/MXene. **e** Normalized K-edge XANES and **f** FT-EXAFS in R space for FeS_2/MXene, FeS_2 QD/MXene and Fe foil. **g–h** Wavelet transforms for the k^3-weighted EXAFS signals of FeS_2/MXene and FeS_2 QD/MXene. **i** Electrostatic potential diagrams of FeS_2 and FeS_2 QD

to the charge delocalization around active sites [42, 43]. As depicted in the K-edge FT-EXAFS in R space (Fig. 2f), the white-line peak intensity of FeS_2 QD/MXene is smaller than that of FeS_2/MXene, which means that charge rearrangement induced by quantum size leads to enhanced electron density in Fe 3*d* orbitals [44]. Furthermore, the coordination distance of FeS_2 QD/MXene (1.65 Å) contributed to Fe–S path significantly larger than that of FeS_2/MXene, and the enhanced bond length implied the optimized delocalized electron regions. As demonstrated in fitting results (Table S1), the FeS_2 QD/MXene curve shows a distinct peak at 3.41 Å attributed to Fe–O–Ti coordination path, demonstrating the strong interfacial coupling between FeS_2 and Ti_3C_2 caused by quantum-size effect [45]. For FeS_2 QD/MXene, the coordination numbers of the Fe–S and Fe–O–Ti paths are, respectively, 5.25, 1.41, and 2.09, which are smaller than those of FeS_2/MXene (6.56 and 2.44), demonstrating the more unsaturated coordination construction in quantum dot structure. The wavelet-transformed (WT) contour plots for Fe K-edge are shown in Figs. 2g–h and S9. The maximum intensity of FeS_2 QD/MXene at 4.05 $Å^{-1}$ is assigned to the Fe–S coordination paths, which is closer to that of FeS_2/MXene, indicating the preserved FeS_2 lattice structure. In addition, another weaker intensity relative maximum at 3.92 $Å^{-1}$ corresponding to appears for FeS_2 QD/MXene. It is evident that quantum-size-induced edge defects

could change the coordination state surrounding Fe atoms, thereby inducing charge delocalization in active sites. The electronic structure optimization is beneficial to promote the multi-electron transition reaction, thus conferring FeS_2 QD/MXene wide-temperature performance superiority.

To further exposure the relationship between electronic structure/properties and electrochemical properties based at atomic scale, the electrostatic potentials, energy band structures and d-band centers have been investigated based on DFT calculations. The optimized model of FeS_2 is constructed in Fig. S10a, and the quantum dot structure was successfully constructed by maximizing the defect concentration at the edge of the FeS_2 lattice (Fig. S10b). In anode materials, when the electronic structure of electrodes could act as a prominent electron donor for coordination with Na^+ ions, the distinctive donor feature was the high negative surface electrostatic potential [46, 47]. As shown in Fig. 2i, the electrostatic potential (ESP) pictures demonstrated the quantum-size effect, and the negative potential was mainly localized around the sulfur atoms in FeS_2 structure. While in FeS_2 QD structure, edge atoms possessed a high number of uncoordinated electrons, preventing the electron conjugated orbital overlap, and results in more negative ESP than that of the intact crystal structure. Hence, the FeS_2 QD structure was more likely to combine with Na^+ and participate in electrochemical reactions. Excellent crystal edge carrier transfer caused electron rearrangement and energy level shift of FeS_2 QD, which plays a vital role in optimizing band structure and regulating band gaps. As a result, FeS_2 QD exhibited a lower band gap value (0.02 eV) compared to integrated FeS_2 structure (0.52 eV) (Fig. S11). Moreover, it can be observed in Fig. S12 that the d-band center (ε_d) of Fe atoms in FeS_2 QD moved from − 2.47 to − 1.20 eV, which was much closer to the Fermi level and contributed to reduce the anti-bonding orbital filling of delocalized electrons, and increase the adsorption strength between active center and Na atoms [48]. In conclusion, the characterization tests and theoretical calculations conjointly proved that the high-concentration unsaturated coordination environment induced by quantum size could enrich electrochemical active centers, providing a possibility for optimizing electrochemical properties and ion diffusion kinetics under wide temperature.

To investigate the collaborative optimization mechanism of quantum-size effect and 3D porous structure on Na^+ storage and transport kinetics, the electrochemical behavior based on prepared MXene, FeS_2/MXene, Fe^{2+}/MXene and FeS_2 QD/MXene anodes was examined in sodium-ion half-cells. As shown in Fig. 3a, the cyclic voltammetry (CV) tests illustrated that a broad reduction peaked at 1.0 V, disappearing in subsequent cycles assigned to the formation of solid electrolyte interface layer (SEI) during the initial Na^+ insertion in FeS_2 QD/MXene anode [49]. Meanwhile, other reduction peaks located at 1.54, 1.14 and 0.76 V, respectively, ascribed to the intercalation of Na^+ into FeS_2 and the subsequent conversion of Na_xFeS_2 into Fe and Na_2S [50]. In the following anodic sweeps, the peak at around 1.58 V could be related to the desodiation of Na_xFeS_2, and oxidation peaks at around 2.17 and 2.7 V might be associated with transformation of FeS_2. What's more, the subsequent CV profiles of the FeS_2 QD/MXene electrode were well overlapped, reflecting its excellent cycle performance and outstanding cycling stability [51].

FeS_2 QD/MXene anode, respectively, delivered initial coulombic efficiency (ICE) of 62.9%, 60.7% and 59.2% at 25, − 35 and 65 °C, which is established in Fig. 3b. The lower ICE is contributed to the electrolyte being more easily decomposed resulting in more side reactions at low or high temperature [52]. As shown in Fig. S13a, the FeS_2 QD/MXene anode possessed the greater ICE and discharged specific capacity in comparison with the MXene (22.6%), FeS_2/MXene (23.7%) and Fe^{2+}/MXene (40.1%) electrodes, demonstrating that the high defect concentration and multiple active centers induced by quantum dot structure possess superior electrochemical reaction activity [53]. Furthermore, the GCD curves overlap well in subsequent cycles, which confirm the excellent stability of FeS_2 QD/MXene electrode for sodium-ion storage. Moreover, the cycling performance of FeS_2 QD/MXene anode at a current density of 0.1 A g^{-1} with the voltage range of 0.01–3.0 V for SIBs at different temperatures is shown in Fig. 3c. After 100 cycles, the well-designed FeS_2 QD/MXene anode could, respectively, deliver high capacities of 463.8, 255.2 and 424.9 mAh g^{-1} under 25, − 35 and 65 °C. On the contrary, an apparent irreversible capacity fading observed in FeS_2/MXene curve (Fig. S13b), which could be attributed to the large FeS_2 particles, would undergo volume expansion during the charge–discharge process, making them prone to detachment from the current collector, and leading to rapid capacity degradation. The MXene and FeS_2 electrodes could, respectively, possess a low specific capacity of 77.2 mAh g^{-1} (Fig. S13) and 58.9 mAh g^{-1} (Fig. S14) at 0.1 A g^{-1} after 100 cycles. But the FeS_2 QD/MXene electrode could deliver a significantly

 https://doi.org/10.1007/s40820-025-01858-2

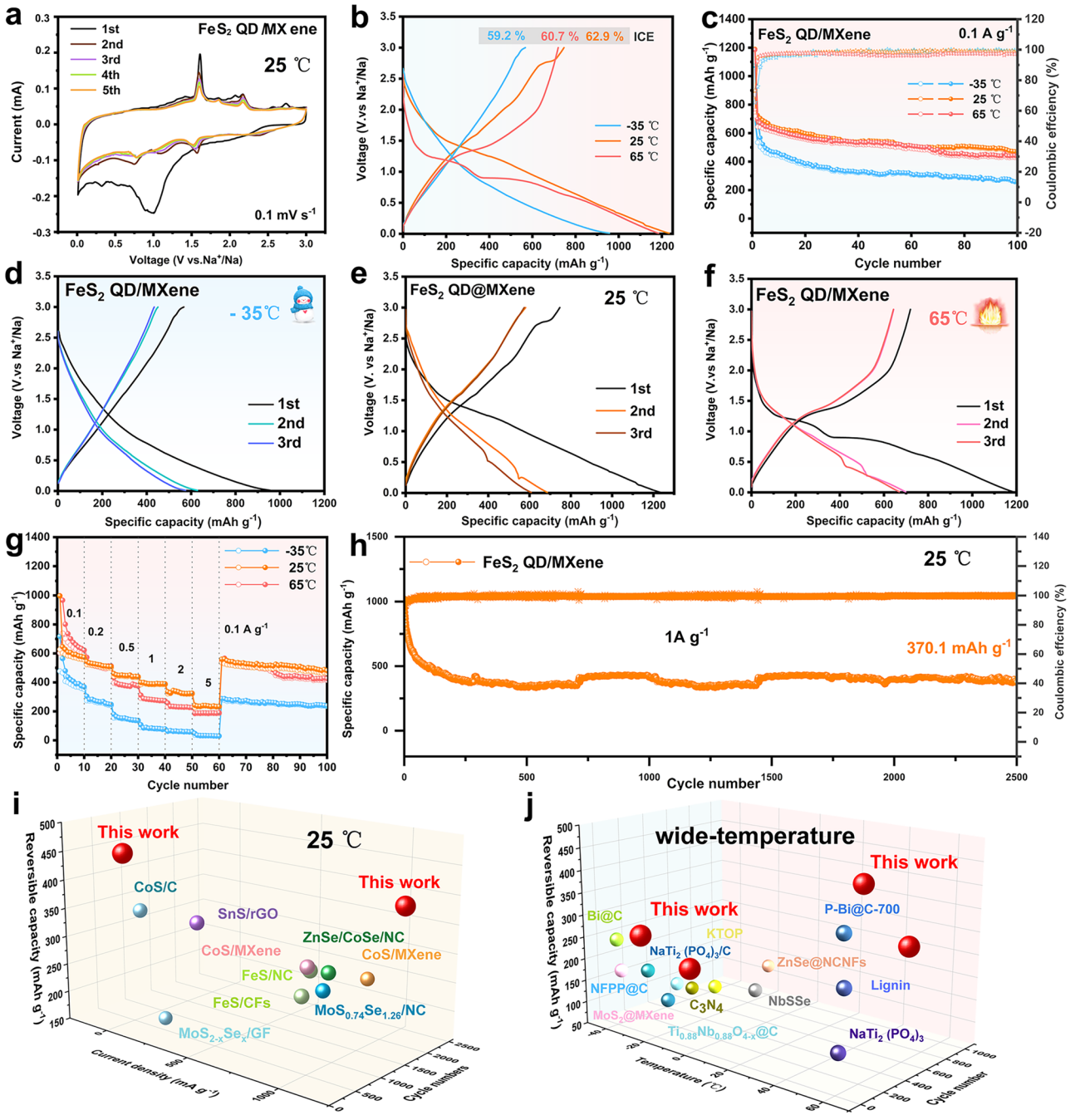

Fig. 3 **a** CV curves at 0.1 mV s^{-1} in 0.01–3.0 V of FeS_2 QD/MXene at 25 °C. **b** GCD curves at first cycle and **c** cycle performance at 0.1 A g^{-1} at different temperatures. GCD profiles for first five cycles at 0.1 A g^{-1} at **d** – 35 °C, **e** 25 °C and **f** 65 °C. **g** Rate capability at increasing current densities at different temperatures. **h** Cycling performance at 1.0 A g^{-1}. **i** Comparison of performance of FeS_2 QD/MXene with the reported TMDs-based anode for SIBs at room temperature and **j** wide temperature

increased capacity of 463.8 mAh g^{-1} at the same current density, which is superior to either single component. Apparently, the improved wide-temperature electrochemical performance was mainly benefiting from the synergistic influence of the three-dimensional hierarchical structure and quantum-size effect. The first three galvanostatic charge/discharge (GCD) profiles of FeS_2 QD/MXene at 0.1 A g^{-1} under wide temperatures are shown in Fig. 3d–f. The first

charge capacity at − 35 °C (951.4 mAh g^{-1}) was lower than the capacity of 1200.2 mAh g^{-1} obtained at 25 °C, which was mainly attributed to the cold service temperature tending to enhance Na^+ ions diffusion barrier, leading to significant capacity fading [54]. Moreover, control experiments under identical low-temperature electrolyte (1 M $NaClO_4$/EC:PC) at − 35 °C are illustrated in Fig. S15; the MXene, FeS_2 QD/MXene and Fe^{2+}/MXene electrodes, respectively, deliver capacities of 20.8, 30.3 and 33.4 mAh g^{-1} after 100 cycles at 0.1 A g^{-1}, which is considerably lower than FeS_2 QD/MXene (255.2 mAh g^{-1}), suggesting that quantum-size effects rather than electrolyte variations drove the improved wide-temperature performance.

The optimized Na^+ transport kinetics in FeS_2 QD/MXene composite were demonstrated by electrochemical impedance spectroscopy (EIS) [55]. As shown in Fig. S16a, the fitting R_{ct} value of FeS_2 QD/MXene (193.0 Ω) was smaller than that of MXene (866.7 Ω), FeS_2/MXene (734.1 Ω) and Fe^{2+}/MXene (628.5 Ω) anodes, indicating the faster ion/electron transfer of abundant edge defects regions. The relationship between impedance and the phase angle is shown in Fig. S16b, and the FeS_2 QD/MXene electrode exhibited the smallest Warburg factor (σ), indicating the fastest Na^+ diffusion efficiency shown in Table S2. The calculated diffusion coefficient of Na^+ ion ($D_{Na}{}^+$, $cm^2\ S^{-1}$) in FeS_2 QD/MXene anode was 1.17×10^{-8} $cm^2\ S^{-1}$, which is higher than that of MXene (6.60×10^{-9} $cm^2\ S^{-1}$), FeS_2/MXene (4.72×10^{-9} $cm^2\ S^{-1}$) and Fe^{2+}/MXene (2.95×10^{-9} $cm^2\ S^{-1}$) electrodes, suggesting that the ultra-fine quantum dot structure could contribute to shorter ions transport distances and enhanced electrolyte penetration for superior charge transfer [56]. Hence, the quantum-sized FeS_2 tended to display significantly rate performance (Fig. 3g), when the current density returns to 0.1 A g^{-1}, the FeS_2 QD/MXene anode still recovered back to deliver excellent capacities of 235.3, 464.3 and 426.1 mAh g^{-1} under − 35/25/65 °C, respectively. The high capacity that achieved adequately reveals prominent fast-charging capability of the FeS_2 QD/MXene anode under wide ambient temperature. And the capacity decay at 65 °C is relatively faster than that at 25 °C, which is due to the instability of the electrolyte at high temperatures.

As shown in Fig. 3h, based on full active sites utilization and fast surface interfacial ion reaction kinetics, the FeS_2 QD/MXene anode exhibited the best long-cycle performance (370.1 mAh g^{-1}) after 2500 cycles at the high current density of 1 A g^{-1}. In contrast, MXene, Fe^{2+}/MXene and FeS_2/MXene electrodes have poor long-term cycling stability, with capacity, respectively, decreasing to 8.6, 33.4 and 132.7 mAh g^{-1} after 1600, 1700 and 1900 cycles (Fig. S17). Obviously, the high concentration of edge uncoordinated electrons induced by quantum-size FeS_2 excites electrochemical activity, attributed to the electrochemical properties of well-designed and also possess superior cycling properties than previous TMD-based electrodes compared with other techniques [S14–S21] (Fig. 3i and Table S3). Besides, the FeS_2 QD/MXene electrode also delivers excellent long-term cycling performance under the wide operation temperatures. As shown in Figs. S18 and S19, after 500 cycles at 0.5 A g^{-1}, the anode, respectively, obtained capacities of 121.5 and 312.5 mAh g^{-1}at -35 and 65 °C. Compared to previously reported works, FeS_2 QD/MXene electrode constructed based on quantum dot effects and 3D MXene skeleton exhibits significant advantages under wide temperature [S22–S33] (Fig. 3j and Table S4).

3.3 Mechanism Investigation

Electrochemical testing has convincingly demonstrated that the integration of unsaturated coordination active sites with regulated heterogeneous structures regulation can synergistically enhance Na^+ storage properties of FeS_2 QD/MXene electrode. To delve deeper into the kinetic mechanism of the prepared FeS_2 QD/MXene anode in SIBs, CV tests are conducted at varying scan rates from 0.1 to 1.2 mV s^{-1}. As illustrated in Fig. 4a, the peak positions and shapes of the CV profiles were consistently preserved across progressively increasing scan rates. The relationship between peak current (i) and scan rate (v) adheres to the following empirical formulas [57]:

$$i = av^b \tag{1}$$

$$\log i = b\log v + \log a \tag{2}$$

where the b approaches 1, the electrochemical reaction is predominantly governed by pseudocapacitance, as well as b-value of 0.5 signifies a purely diffusion-dominated process. The calculated b-values of FeS_2 QD/MXene electrode are shown in Fig. 4b. Compared with the Fe^{2+}/MXene (Fig. S20), FeS_2/MXene (Fig. S21) and MXene (Fig. S22)

https://doi.org/10.1007/s40820-025-01858-2

anodes, the FeS_2 QD/MXene electrode was mainly based on the highly active hetero-interface-induced capacitance process control for Na^+ ions storage, which exhibits enhanced charge transport characteristics. In addition, the capacitive contribution ratio can be estimated according to following equations [58]:

$$i = k_1 v + k_2 v^{\frac{1}{2}} \tag{3}$$

$$\frac{i}{v^{\frac{1}{2}}} = k_2 v^{\frac{1}{2}} + k_1 \tag{4}$$

in which $k_1 v$ and $k_2 v^{\frac{1}{2}}$, respectively, stand for the pseudocapacitive process and diffusion-dominated processes. As depicted in Fig. 4c, d, it can be concluded that the contribution of the pseudocapacitance-controlled behavior increases as the scan rate increases from 0.1 to 1.2 mV s^{-1}. When the scan rate achieves 1.2 mV s^{-1}, the dominating capacitive contribution of FeS_2 QD/MXene electrode depicted a value of 77.0%, significantly surpassing those of the Fe^{2+}/MXene (68.9% at 1.2 mV s^{-1}), FeS_2/MXene (51.9% at 1.0 mV s^{-1}) and MXene (39.2% at 1.0 mV s^{-1}) anodes. The high pseudocapacitance contribution could be related to the

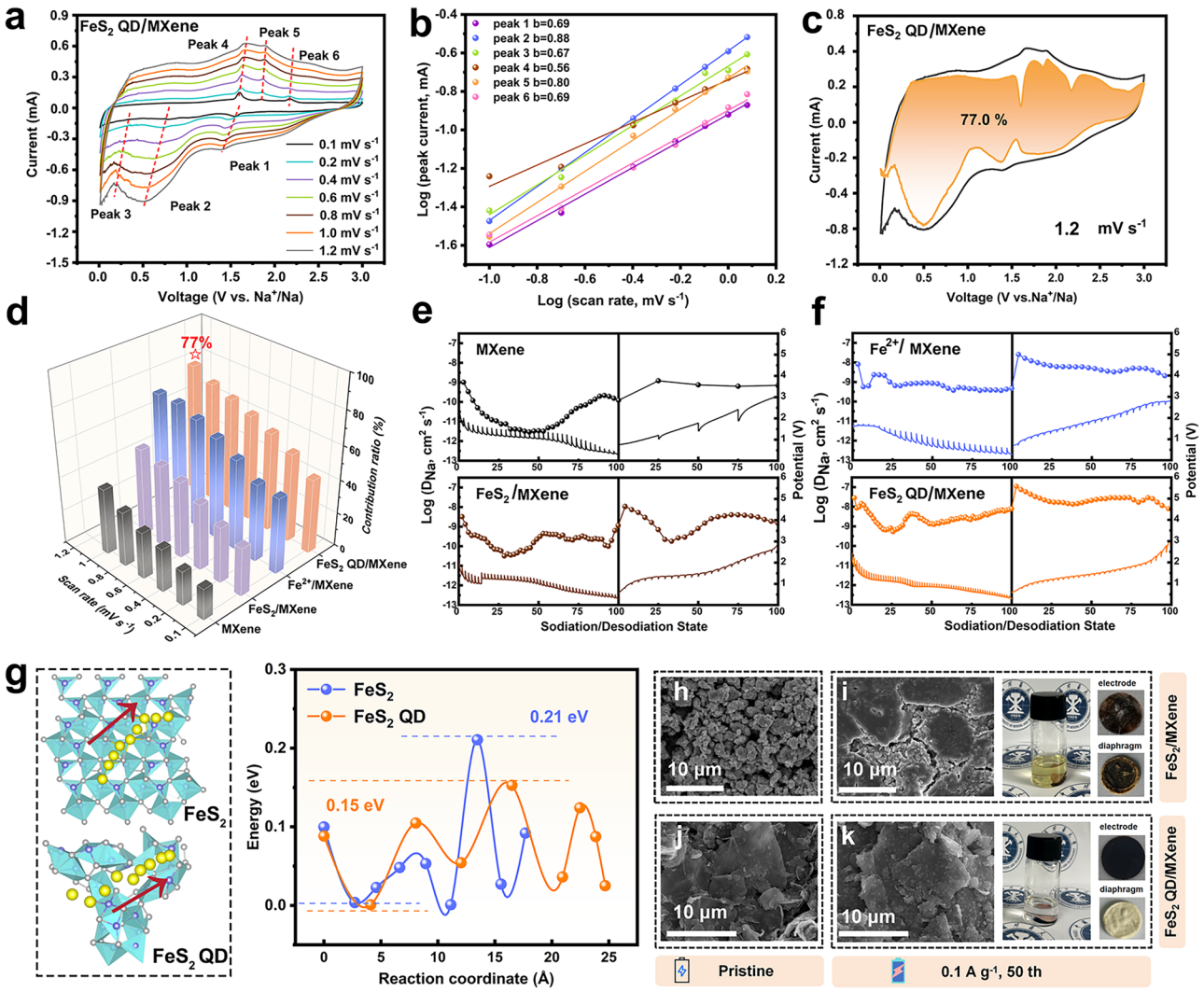

Fig. 4 **a** CV curves at different scan rates. **b** Linear relationship of peak currents versus scan rates. **c** Capacitive contribution curve for FeS_2 QD/MXene anode at 1.0 mV s^{-1}. **d** Capacitive contribution ratios and **e–f** GITT potential profiles and Na^+ ions diffusion system of electrodes. **g** Na^+ ions diffusion routes across and the corresponding diffusion energies of FeS_2 and FeS_2 QD/MXene electrodes. **h–k** SEM images, post cycled electrodes/separators photographs after cycling of FeS_2/MXene and FeS_2 QD/MXene anodes

uncoordinated active sites and fast-ion diffusion transport, which due to the high-concentration edge defects, strong interfacial coupling and highly efficient charge transport of FeS_2 QD/MXene composites, contributing to excellent electrochemical reaction kinetics. Hence, the FeS_2 QD/MXene anode showed much higher D_{Na}^+ kinetics than other electrodes (Figs. 4e, f and S23). The FeS_2 QD/MXene electrode also exhibits fast Na^+ ions transport over wide-temperature range, the GITT curves are shown in Figs. S24 and S25. In particular, the D_{Na}^+ at − 35 °C is only two orders of magnitude lower than that of room temperature, which further confirming that unsaturated coordinated edge atoms of FeS_2 QDs could significantly enhance the Na^+ diffusion behaviors. Moreover, DFT calculations were also conducted to explore the sodium migration phenomenon, with the optimized migration paths exhibited in Fig. 4g. Compared with the integrated FeS_2 lattice structure, the FeS_2 QD structure featured a higher concentration of edge uncoordinated atoms and grain boundary active sites. The migration paths indicated that Na atoms navigating through the FeS_2 QD structure were less restricted by the intrinsic lattice constraints, thus exhibiting greater diffusion freedom and delocalization possibilities. This structural advantage likely facilitates the formation of Na_2S at defect-rich edge sites, resulting in lower diffusion barriers (0.15 eV) and promoting low-impedance Na^+ migration [59].

To further elucidate this reaction process, cells after cycling were disassembled to demonstrate electrode morphology and diaphragm state. In Figs. 4h-k and S26, the MXene, FeS_2/MXene, Fe^{2+} MXene anodes exhibited obvious agglomeration and fragmentation after charging/discharging process with severe electrode splitting. In comparison, the FeS_2 QD/MXene anode maintained structural integrity after 50 cycles at 0.1 A g^{-1}, accounting for its exceedingly electrochemical performance and long-cycle stability. Additionally, cross-sectional SEM images revealed that the FeS_2/MXene anode is dislodged from the fluid collector and the cross-sectional thickness expansion of up to 52.1% (Fig. S27), compared to only 16.2% for the FeS_2 QD/MXene electrode (Fig. S28). As depicted in Fig. 4h, i, when recycled electrodes were immersed in the fresh electrolyte, the FeS_2/MXene anode presented a cloudy appearance, indicative of a significant shuttle effect. In contrast, distinct yellow deposits were observed on the glass fiber separator of FeS_2/MXene after cycling. On the contrary, the electrolyte containing FeS_2 QD/MXene anode remained transparent suggesting effective inhibition of the polysulfide shuttle effect (Fig. 4j, k). The innovative design of the FeS_2 QD/MXene electrode, featuring unsaturated coordination structures, likely induces local electron delocalization, thereby enhancing charge conversion capabilities and inhibiting the formation of polysulfides and by-products.

To comprehensively examine the sodium storage and transport mechanisms of FeS_2 QD/MXene composite, the ex situ XRD patterns during the first cycle of charging/discharging cycle are shown in Fig. 5a. The distinct reflections from the Ti_3C_2 material were observed at 6.2° and 19.4°, corresponding to the (002) and (006) planes, respectively, in the initial state of discharge. As the discharge progressed, the positions of these diffraction peaks gradually shifted toward smaller angles, with a concurrent reduction in intensity, indicating the insertion of Na^+ ions into the interlayers of the MXene substrate. Notably, upon recharging the electrode to 3.0 V, these peaks reverted to their original positions, demonstrating a highly reversible conversion reaction. Further insights into the conversion reaction mechanism of the FeS_2 QD/MXene anode were sought through ex situ Raman spectroscopy (Fig. 5b). During the discharge proceeding, the peaks emerging at around 218.3 cm^{-1} gradually appear, which could be attributed to the formation of Na_2S [60]. Notably, at a discharge voltage of 0.01 V, the peak associated with the Na–S bond reached maximum intensity, whereas the Fe–S peak at approximately 280 cm^{-1} nearly vanished, indicating rapid charge transport within the FeS_2 QD. This charge interaction appears to facilitate the coordination of Na^+ ions, enhancing the conversion reaction that produces Na_2S. Upon charging the electrode to 3.0 V, the peak indicative of the Na–S bond disappeared, and the Fe–S bond peak reappeared, suggesting the reversible regeneration of the active FeS_2 material. Additionally, peaks at 631.0 cm^{-1}, attributed to Ti–C bonds, were observed to red shift to 612.2 cm^{-1} during the discharge process, confirming the successful embedding of Na^+ ions and the consequent expansion of the MXene interlayer spacing [61]. Crucially, during the subsequent charging process, the peak position fully reverts to its original value of 631.0 cm^{-1}, demonstrating Na^+ deintercalation and confirming the highly reversible nature of the structural changes.

To examine the morphological and microstructural changes during the sodiation/desodiation processes of the FeS_2 QD/MXene anode, ex situ TEM was employed. Upon discharging the electrode to 0.01 V, HRTEM images

 https://doi.org/10.1007/s40820-025-01858-2

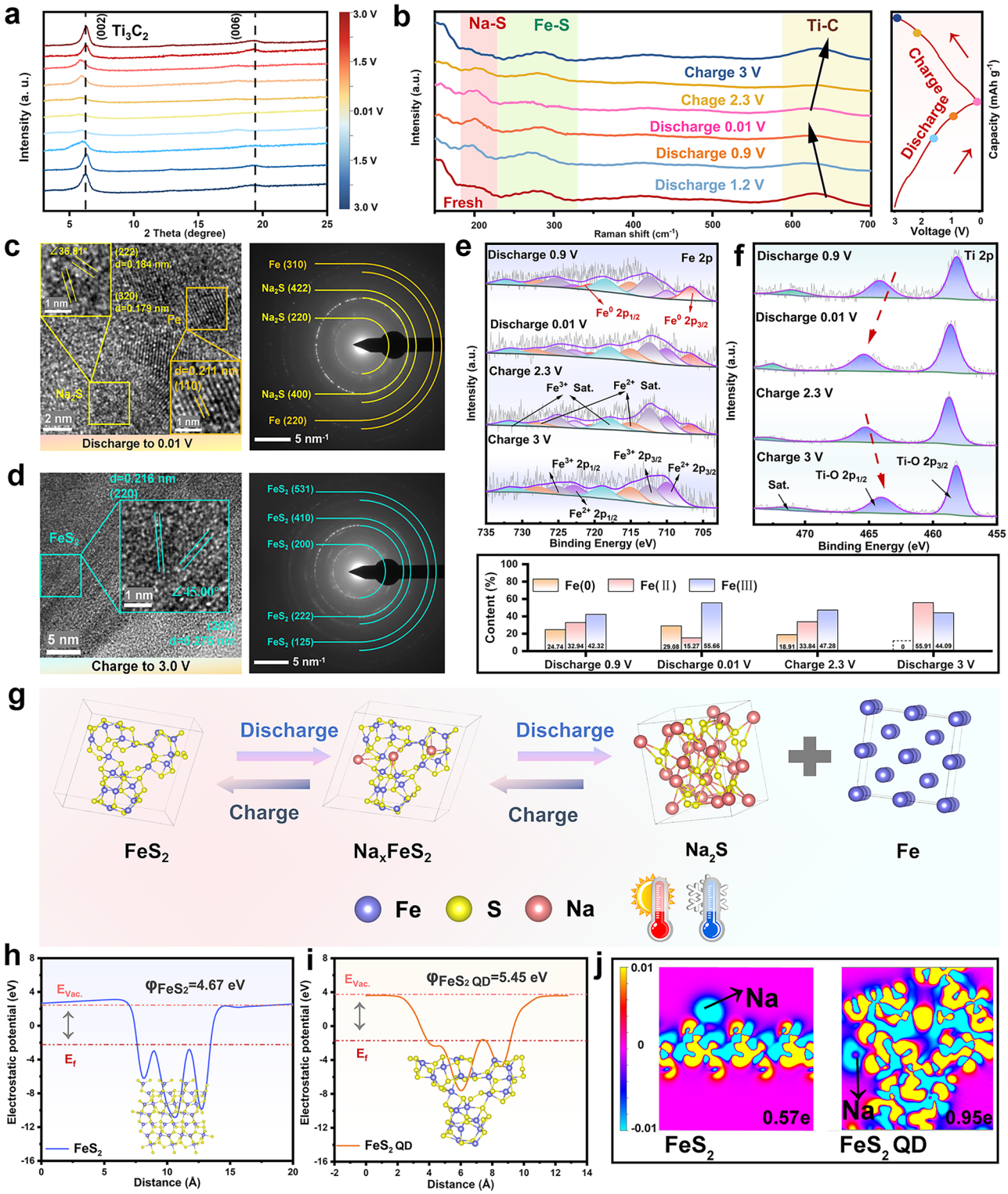

Fig. 5 **a** Ex situ XRD, **b** ex situ Raman spectra, **c-d** ex situ TEM images and **e–f** ex situ XPS of FeS_2 QD/MXene electrodes at different discharge/charge voltages at first cycle. **g** Schematic illustration of sodium storage mechanism based on FeS_2 QD/MXene electrode. **h–i** Work functions and **j** 2D charge difference plots of FeS_2 and FeS_2 QD structures

revealed the emergence of lattice fringes corresponding to the Na_2S crystal planes of (222) and (320) (Fig. 5c). Additionally, lattice fringes associated with the (110) plane of metallic Fe were also observed. Importantly, the formation of Fe and Na_2S hetero-interfaces during discharge appears to facilitate space charge storage at these interfaces, enhancing localized charge redistribution. This enhancement contributes to interfacial pseudocapacitance and stabilizes the reaction kinetics [62]. Furthermore, SAED analysis displayed distinct diffraction rings for the (310) and (220) planes of Fe, as well as the (442), (220), and (400) planes of Na_2S, consistent with the ex situ XRD patterns. Conversely, upon charging the electrode to 3.0 V, the lattice fringes corresponding to Fe and Na_2S disappeared (Fig. 5d), with those corresponding to the (220) and (200) crystal planes of FeS_2 reemerging, indicating excellent reversibility of the composite electrode. This reversible disappearance of hetero-interfaces further confirms the dynamic nature of space charge storage, synergizing with electrode conversion reactions to achieve high reversibility [63, 64]. This dual mechanism underscores the structural and electrochemical benefits of the FeS_2 QD/MXene architecture.

Additionally, ex situ XPS was conducted to analyze the states of the FeS_2 QD/MXene electrode at various charging and discharging stages. As shown in Fig. 5e, during the Na^+ insertion process, peaks at 706.1 and 720.5 eV attributed to the Fe element of the discharge product were consistently present, reaching their maximum intensity (29.08%) at a potential of 0.01 V. The disappearance of these Fe element peaks and the elevated level of Fe (II) after charging to 3.0 V suggests the re-formation of FeS_2. Moreover, the emergence of peaks attributed to Fe(III) $2p_{3/2}$ and Fe(III) $2p_{1/2}$ indicates the formation of less active Fe(III) oxides on the electrode surface, likely due to irreversible electrolyte side reactions during the initial charge/discharge cycle. Peaks at 458.12 and 464.07 eV, respectively, corresponding to the Ti–O $2p_{3/2}$ and Ti–O $2p_{3/1}$ orbitals were identified, linked to the Ti atom in the FeS_2 QD/MXene electrode (Fig. 5f). When discharged to 0.01 V, these two peaks shifted to 458.33 and 464.30 eV, suggesting that the Ti–O functional groups had captured Na^+ ions during sodiation process [65]. When recharged to 3.0 V, the peaks associated with the Ti–O bond returned to lower binding energies, confirming the excellent reversibility of the FeS_2 QD/MXene electrode. The above discussions systematically clarify the Na^+ electrochemical reaction mechanism in the FeS_2 QD/MXene, as depicted in Fig. 5g, and the transformation reaction equations are summarized as follows:

$$FeS_2 + xNa^+ + xe^- \leftrightarrow Na_xFeS_2 \quad (5)$$

$$Na_xFeS_2 + (4-x)Na^+ + xe^- \leftrightarrow 2Na_2S + Fe \quad (6)$$

First-principles calculations were performed to elucidate the mechanisms underlying the highly reversible conversion reaction of the FeS_2 QD/MXene electrode. The work function results presented in Fig. 5h, i indicate a greater propensity for electron transfer from the integrated FeS_2 and FeS_2 QD to the adsorption surface. Compared to FeS_2 crystals, which have a work function of 4.67 eV, the FeS_2 QD exhibits an increased work function of 5.32 eV. This increase demonstrates that the quantum-sized structure disrupts the electrochemical inertia of the basal plane atoms, facilitating the transfer of internal electrons to the surface of the FeS_2 QD [66]. The quantum-size effect modifies the electronic energy and optimizes the surface charge distribution, thus lowering the Na^+ diffusion energy barrier. This aligns with the observed low R_{ct} and high rate performance in electrochemical tests conducted at various temperatures. Additionally, 2D differential charge density calculations quantify the localized electron enrichment phenomenon at the FeS_2 QD/MXene electrode. As depicted in Fig. 5j, the Bader charge transfer between the FeS_2 QD and Na atoms reaches 0.95 e, significantly exceeding the 0.57 e of bulk FeS_2. These findings confirm that charge delocalization and high-concentration defects, driven by the quantum-size effect, contribute to significant improvements in cycling performance and rapid ion diffusion across wide temperature.

Moreover, to investigate the composition and vertical distribution of the SEI after cycling at different temperatures, XPS depth profiling on anodes after 10 cycles was performed (Fig. 6). C 1*s* spectra revealed peaks corresponding to C–C/C–H (284.8 eV), C–O (286.2 eV) and C=O (290.5 eV) at both 25 and − 35 °C (Fig. 6a, b). Cycling at 65 °C, however, introduced an additional peak at ~ 292.0 eV, assigned to O=C–O species, potentially yielded by decarboxylation of the DMC solvent under rising temperature (Fig. 6c) [54]. Analysis of F 1*s* spectra ascertained the components due to $Na_xPF_yO_z$/Na_xPF_y at ~ 688.0 eV and Na–F bonds at ~ 685.0 eV. The intensity of the P–F-signal was

https://doi.org/10.1007/s40820-025-01858-2

notably lower at − 35 °C compared to that at room temperature (Fig. 6d, e). This suppression can be explained by restricted ion diffusion at low temperature, stimulating SEI reorganization into a NaF-dominated structure that immensely reduces the desolvation energy barrier [67]. Conversely, P–F bond intensity at 65 °C recovered to levels comparable to ambient conditions (Fig. 6f), suggesting that phosphorus-containing fluorides were reformed by thermally induced electrolyte decomposition [68]. S 2*p* spectra at 25 °C displayed surface enrichment of oxidized sulfur species of Na_2SO_3, Na_2SO_4, which diminished after sputtering, alongside Na_2S and Na_2S_x (Fig. 6g). At − 35 °C, the migration of SO_3 and Na_2S hampered by restricted diffusion stabilized the sulfur speciation profile throughout etching (Fig. 6h) [69]. In contrast, in addition to bolstering electrode activity, elevated temperature encouraged the decomposition of SO_4^{2-}/SO_3^{2-} into Na_2S/Na_2S_x and spurred the reduction of organic sulfur (Fig. 6i) [70].

The ion-induced method presented in this study offers a viable approach for the in situ growth of various TMD-based quantum dots on 3D MXene substrates, such as CoS_2 QD (Fig. S29). Leveraging the unique quantum structure, CoS_2 QD/MXene and NiS_2 QD/MXene deliver reversible capacities of 285.2 and 255.8 mAh g^{-1}, respectively, after 100 cycles at a current of 0.1 A g^{-1}, when used as SIB anodes. Additionally, DFT calculations indicate a significant

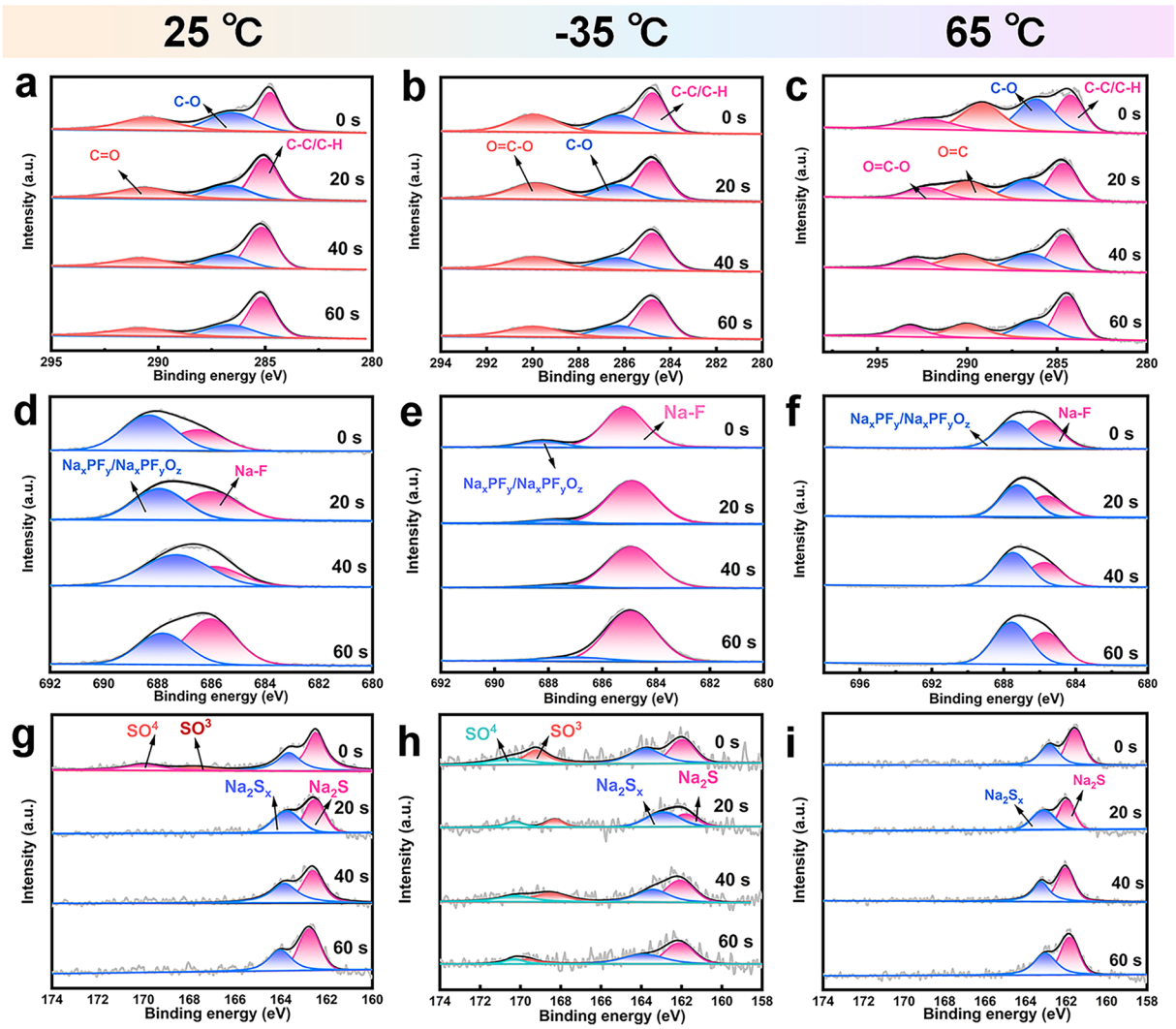

Fig. 6 In-depth **a–c** C 1*s*, **d–f** F 1*s* and **g–i** S 2*p* of FeS_2 QD/MXene electrode after 10 cycles with the sputter time of 0, 20, 40, and 60 s under 25, − 35 and 65 °C

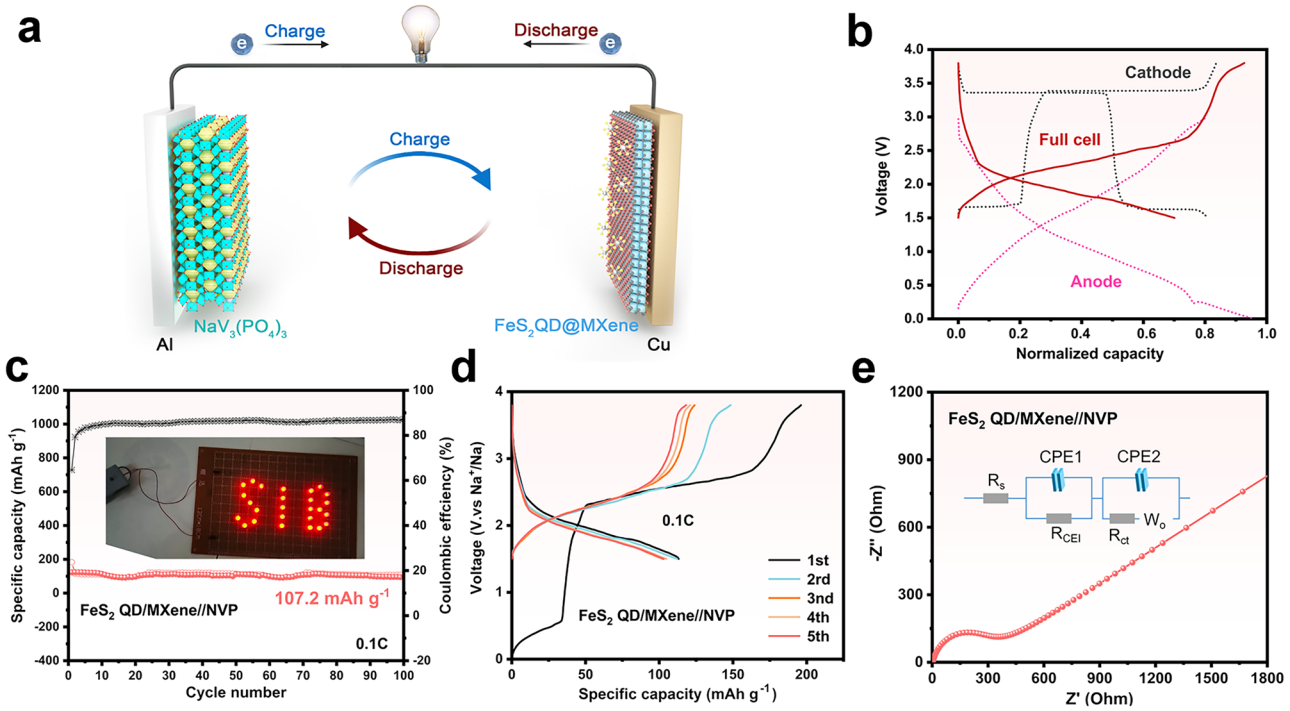

Fig. 7 **a** Schematic illustration of the sodium full battery constructed by NVP cathode and FeS_2 QD/MXene anode. **b** Charge and discharge curves, **c** cycling stability, **d** GCD profiles for the first five cycles at 0.1 C and **e** Nyquist pots of the FeS_2 QD/MXene//NVP SIB

increase in the Na^+ adsorption energy, from − 0.53 eV in pristine SnS to − 1.51 eV in SnS QD (Fig. S30). This enhancement clearly demonstrates the crucial roles of quantum confinement and MXene hybridization in improving interfacial interactions across different metal sulfides. This work introduces an effective and general defect regulation strategy that holds promise for the development of superior TMD-based electrodes for sodium-ion batteries. To further demonstrate the practical application potential of the FeS_2 QD/MXene electrode, a full cell was constructed using a FeS_2 QD/MXene anode and a $Na_3V_2(PO4)_3$ (NVP) cathode (Fig. 7a). The sodium-ion half-cell cycling performance, using an NVP cathode, is documented in Fig. S31, displaying a stable reversible capacity of 65 mAh g^{-1} after 100 cycles at 0.1 A g^{-1}. To ensure a balanced capacity between the cathode and anode, the mass ratio of cathode-to-anode active materials in the full cell was maintained at approximately 3:1, with an anode mass loading of 1.1 mg. As shown in Fig. 7b, the output voltage range of the FeS_2 QD/MXene// NVP SIB could be determined by the charge/discharge profiles of normalized capacity, and the range of working voltages were finally set as 1.5 ~ 3.8 V to ensure stable operation of the full cell. The FeS_2 QD/MXene//NVP full cell exhibited relatively great stability (Fig. 7c), retaining 107.2 mAh g^{-1} of the capacity at 0.1 C after 100 cycles. Figure 7d presents the GCD curves for the first five cycles, indicating a well-preserved initial shape and suggesting an excellent match between the cathode and anode. Notably, Fig. S32 shows that at a temperature of − 35 °C, the full cell achieves a high energy density of 162.4 Wh kg^{-1} and a power density of 324.8 W kg^{-1}. Subsequent EIS tests confirmed that the assembled full cell exhibits low interface impedance and superior ion transport performance (Fig. 7e), underscoring its potential for practical applications.

4 Conclusions

In summary, an ion-diffusion-enhanced FeS_2 QD/MXene anode with a unique delocalized electronic regions has been constructed for high sodium storage under wide temperatures. DFT calculations revealed that quantum-size effects enriched edge uncoordinated centers in FeS_2, promoting charge delocalization at the atomic scale and optimizing electronic structure for accelerated charge transport.

https://doi.org/10.1007/s40820-025-01858-2

Moreover, the tightly connected of 3D skeleton and FeS_2 QD produced excellent dispersibility and the highly stable electrode, which shortened the ions transport distance and facilitated the electrons transfer. Benefiting from the ideal edge electron concentration and strong interfacial coupling, the FeS_2 QD/MXene anode delivers a high reversible capacity of 255.2 mAh g^{-1} at − 35 °C and 424.9 mAh g^{-1} at 65 °C after 100 cycles. Furthermore, the FeS_2 QD/MXene//NVP full cell exhibits a 71.5% capacity retention (relative to that at 25 °C) after 100 cycles, indicating its high potential for practical use under wide-temperature conditions. This study not only provides insights into efficient Na^+ storage and transport mechanisms but also offers a universal strategy for other TMD-based materials (e.g., CoS_2 QD, NiS_2 QD, and SnS QD). By shedding light on the design of quantum-scale structure and electron delocalization, this work makes it possible for developing high energy density sodium energy storage devices at wide temperature.

Acknowledgements This work was financially supported by the National Nature Science Foundation of China (Nos. 52202335 and 52171227) and Natural Science Foundation of Jiangsu Province (No. BK20221137) and National Key R&D Program of China (2024YFE0108500).

Author Contributions Tianlin Li and Danyang Zhao did writing—review and editing, writing—original draft, methodology, investigation, and conceptualization. Meiyu Shi performed methodology and investigation. Chao Tian and Jie Yi did formal analysis. Yongzhi Li, Qing Yin, Bin Xiao, Jiqiu Qi, Peng Cao and Yanwei Sui reviewed the article. All authors have given approval to the final version of the manuscript.

Declarations

Conflict of interest The authors declare no conflict of interest. They have no known competing financial interests or personal relationships that could have appeared to influence the work reported in this paper.

Supplementary Information The online version contains supplementary material available at https://doi.org/10.1007/s40820-025-01858-2.

References

1. J. Hu, X. Li, Q. Liang, L. Xu, C. Ding et al., Optimization strategies of $Na_3V_2(PO_4)_3$ cathode materials for sodium-ion batteries. Nano-Micro Lett. **17**(1), 33 (2024). https://doi.org/10.1007/s40820-024-01526-x
2. Z. Nan, W. Wei, Z. Lin, R. Yuan, M. Zhang et al., Electromagnetic functions modulation of recycled by-products by heterodimensional structure. Nano-Micro Lett **17**(1), 137 (2025). https://doi.org/10.1007/s40820-025-01659-7
3. Z.P. Cano, D. Banham, S. Ye, A. Hintennach, J. Lu et al., Batteries and fuel cells for emerging electric vehicle markets. Nat. Energy **3**(4), 279–289 (2018). https://doi.org/10.1038/s41560-018-0108-1
4. M. Jiang, P. Wang, Q. Chen, Y. Zhang, Q. Wu et al., Enabling the Nb/Ti co-doping strategy for improving structure stability and rate capability of Ni-rich cathode. Chin. Chem. Lett. **36**(6), 110040 (2025). https://doi.org/10.1016/j.cclet.2024.110040
5. Z. Li, Y.-X. Yao, S. Sun, C.-B. Jin, N. Yao et al., 40 years of low-temperature electrolytes for rechargeable lithium batteries. Angew. Chem. Int. Ed. **62**(37), e202303888 (2023). https://doi.org/10.1002/anie.202303888
6. Y. Li, R. Zhang, J. Qian, Y. Gong, H. Li et al., Construct NiSe/NiO heterostructures on NiSe anode to induce fast kinetics for sodium-ion batteries. Energy Mater. Adv. **4**, 0044 (2023). https://doi.org/10.34133/energymatadv.0044
7. A. Nagmani, S. Kumar, Puravankara, Optimizing ultramicroporous hard carbon spheres in carbonate ester-based electrolytes for enhanced sodium storage in half-/full-cell sodium-ion batteries. Battery Energy **1**(3), 20220007 (2022). https://doi.org/10.1002/bte2.20220007
8. Q. Wang, C. Guo, Y. Zhu, J. He, H. Wang, Reduced graphene oxide-wrapped FeS_2 composite as anode for high-performance sodium-ion batteries. Nano-Micro Lett. **10**(2), 30 (2018). https://doi.org/10.1007/s40820-017-0183-z
9. Y. Gong, Y. Li, Y. Li, M. Liu, X. Feng et al., Unraveling the intrinsic origin of the superior sodium-ion storage performance of metal selenides anode in ether-based electrolytes. Nano Lett. **24**(27), 8427–8435 (2024). https://doi.org/10.1021/acs.nanolett.4c02145
10. Y.-F. Zhu, Y. Xiao, W.-B. Hua, S. Indris, S.-X. Dou et al., Manipulating layered P2@P3 integrated spinel structure evolution for high-performance sodium-ion batteries. Angew. Chem. Int. Ed. **59**(24), 9299–9304 (2020). https://doi.org/10.1002/anie.201915650
11. Z. Ali, T. Zhang, M. Asif, L. Zhao, Y. Yu et al., Transition metal chalcogenide anodes for sodium storage. Mater. Today **35**, 131–167 (2020). https://doi.org/10.1016/j.mattod.2019.11.008

12. Z. Zhu, T. Jiang, M. Ali, Y. Meng, Y. Jin et al., Rechargeable batteries for grid scale energy storage. Chem. Rev. **122**(22), 16610–16751 (2022). https://doi.org/10.1021/acs.chemrev.2c00289
13. B. Sun, Q. Lu, K. Chen, W. Zheng, Z. Liao et al., Redox-active metaphosphate-like terminals enable high-capacity MXene anodes for ultrafast Na-ion storage. Adv. Mater. **34**(15), 2108682 (2022). https://doi.org/10.1002/adma.202108682
14. Y. Fang, X. Lv, Z. Lv, Y. Wang, G. Zheng et al., Electron-extraction engineering induced 1T''-1T' phase transition of $Re_{0.75}V_{0.25}Se_2$ for ultrafast sodium ion storage. Adv. Sci. **9**(36), 2205680 (2022). https://doi.org/10.1002/advs.202205680
15. J. Holoubek, H. Liu, Z. Wu, Y. Yin, X. Xing et al., Tailoring electrolyte solvation for Li metal batteries cycled at ultra-low temperature. Nat. Energy (2021). https://doi.org/10.1038/s41560-10.1038/s41021-00783-z(2021).10.1038/s41560-021-00783-z
16. M. Wang, H. Xu, Z. Yang, H. Yang, A. Peng et al., SnS nanosheets confined growth by S and N codoped graphene with enhanced pseudocapacitance for sodium-ion capacitors. ACS Appl. Mater. Interfaces **11**(44), 41363–41373 (2019). https://doi.org/10.1021/acsami.9b14098
17. T. Li, D. Zhao, B. Du, Q. Yin, Y. Li et al., Defect-induced electron rich nanodomains in CoSe0.5S1.5/GA realize fast ion migration kinetics as sodium-ion capacitor anode. J. Energy Chem. **87**, 583–593 (2023). https://doi.org/10.1016/j.jechem.2023.10.011
18. P. Wang, D. Zhao, X. Hui, Z. Qian, P. Zhang et al., Bifunctional catalytic activity guided by rich crystal defects in Ti_3C_2 MXene quantum dot clusters for Li–O_2 batteries. Adv. Energy Mater. **11**(32), 2003069 (2021). https://doi.org/10.1002/aenm.202003069
19. H. Zhu, W. Zan, W. Chen, W. Jiang, X. Ding et al., Defect-rich molybdenum sulfide quantum dots for amplified photoluminescence and photonics-driven reactive oxygen species generation. Adv. Mater. **34**(31), 2200004 (2022). https://doi.org/10.1002/adma.202200004
20. Z. Lv, B. Peng, X. Lv, Y. Gao, K. Hu et al., Intercalative motifs-induced space confinement and bonding covalency enhancement enable ultrafast and large sodium storage. Adv. Funct. Mater. **33**(16), 2214370 (2023). https://doi.org/10.1002/adfm.202214370
21. J. Bai, J.H. Jia, Y. Wang, C.C. Yang, Q. Jiang, Ideal bi-based hybrid anode material for ultrafast charging of sodium-ion batteries at extremely low temperatures. Nano-Micro Lett. **17**(1), 60 (2024). https://doi.org/10.1007/s40820-024-01560-9
22. X. Sun, L. Wang, C. Li, D. Wang, I. Sikandar et al., Dandelion-Like Bi_2S_3/rGO hierarchical microspheres as high-performance anodes for potassium-ion and half/full sodium-ion batteries. Nano Res. **14**(12), 4696–4703 (2021). https://doi.org/10.1007/s12274-021-3407-y
23. X. Xu, D. Feng, L. You, Y. Xie, F. Wu et al., Carbon-encrusted SnS_2Decorated on MXene nanosheets for advanced Li-ion battery anodes. Energy Mater. Adv. **5**, 0146 (2024). https://doi.org/10.34133/energymatadv.0146
24. M. Naguib, V.N. Mochalin, M.W. Barsoum, Y. Gogotsi, Two-dimensional materials: 25th anniversary article: MXenes: a new family of two-dimensional materials. Adv. Mater. **26**(7), 982–982 (2014). https://doi.org/10.1002/adma.201470041
25. J. Orangi, M. Beidaghi, A review of the effects of electrode fabrication and assembly processes on the structure and electrochemical performance of 2D MXenes. Adv. Funct. Mater. **30**(47), 2005305 (2020). https://doi.org/10.1002/adfm.202005305
26. J. Zhang, Y. Yan, X. Wang, Y. Cui, Z. Zhang et al., Bridging multiscale interfaces for developing ionically conductive high-voltage iron sulfate-containing sodium-based battery positive electrodes. Nat. Commun. **14**(1), 3701 (2023). https://doi.org/10.1038/s41467-023-39384-7
27. Y. Liu, M. Qiu, X. Hu, J. Yuan, W. Liao et al., Anion defects engineering of ternary Nb-based chalcogenide anodes toward high-performance sodium-based dual-ion batteries. Nano-Micro Lett. **15**(1), 104 (2023). https://doi.org/10.1007/s40820-023-01070-0
28. L. Zhang, W. Zhao, S. Yuan, Y. Yang, P. Ge et al., Tailoring MSx quantum dots (M = co, Ni, Cu, Zn) for advanced energy storage materials with strong interfacial engineering. Small **18**(10), 2106593 (2022). https://doi.org/10.1002/smll.202106593
29. Y. Deng, T. Shang, Z. Wu, Y. Tao, C. Luo et al., Fast gelation of $Ti_3C_2T_x$ MXene initiated by metal ions. Adv. Mater. **31**(43), 1902432 (2019). https://doi.org/10.1002/adma.201902432
30. G. Zhou, M.-C. Li, C. Liu, C. Liu, Z. Li et al., 3D printed nitrogen-doped thick carbon architectures for supercapacitor: ink rheology and electrochemical performance. Adv. Sci. **10**(10), 2206320 (2023). https://doi.org/10.1002/advs.202206320
31. Y. Wang, Y. Zhang, J. Shi, A. Pan, F. Jiang et al., S-doped porous carbon confined SnS nanospheres with enhanced electrochemical performance for sodium-ion batteries. J. Mater. Chem. A **6**(37), 18286–18292 (2018). https://doi.org/10.1039/C8TA06106H
32. Z. Hu, Z. Zhu, F. Cheng, K. Zhang, J. Wang et al., Pyrite FeS_2 for high-rate and long-life rechargeable sodium batteries. Energy Environ. Sci. **8**(4), 1309–1316 (2015). https://doi.org/10.1039/c4ee03759f
33. D. Zhao, P. Wang, H. Di, P. Zhang, X. Hui et al., Single semi-metallic selenium atoms on Ti_3C_2 MXene nanosheets as excellent cathode for lithium–oxygen batteries. Adv. Funct. Mater. **31**(29), 2010544 (2021). https://doi.org/10.1002/adfm.202010544
34. S. Li, H. Zhu, Y. Liu, Z. Han, L. Peng et al., Codoped porous carbon nanofibres as a potassium metal host for nonaqueous K-ion batteries. Nat. Commun. **13**(1), 4911 (2022). https://doi.org/10.1038/s41467-022-32660-y
35. C. Ma, X. Wang, J. Lan, J. Zhang, K. Song et al., Dynamic multistage coupling of FeS_2/S enables ultrahigh reversible Na–S batteries. Adv. Funct. Mater. **33**(5), 2211821 (2023). https://doi.org/10.1002/adfm.202211821

 https://doi.org/10.1007/s40820-025-01858-2

36. K. Shevchuk, A. Sarycheva, C.E. Shuck, Y. Gogotsi, Raman spectroscopy characterization of 2D carbide and carbonitride MXenes. Chem. Mater. **35**(19), 8239–8247 (2023). https://doi.org/10.1021/acs.chemmater.3c01742
37. A. Sarycheva, Y. Gogotsi, Raman spectroscopy analysis of the structure and surface chemistry of $Ti_3C_2T_x$ MXene. Chem. Mater. **32**(8), 3480–3488 (2020). https://doi.org/10.1021/acs.chemmater.0c00359
38. H. Wang, X. Song, M. Lv, S. Jin, J. Xu et al., Interfacial covalent bonding endowing Ti_3C_2-Sb_2S_3 composites high sodium storage performance. Small **18**(3), e2104293 (2022). https://doi.org/10.1002/smll.202104293
39. J. Halim, S. Kota, M.R. Lukatskaya, M. Naguib, M.-Q. Zhao et al., Synthesis and characterization of 2D molybdenum carbide (MXene). Adv. Funct. Mater. **26**(18), 3118–3127 (2016). https://doi.org/10.1002/adfm.201505328
40. C. Yue, X. Zhang, J. Yin, H. Zhou, K. Liu et al., Highly efficient FeS_2@FeOOH core-shell water oxidation electrocatalyst formed by surface reconstruction of FeS_2 microspheres supported on Ni foam. Appl. Catal. B Environ. **339**, 123171 (2023). https://doi.org/10.1016/j.apcatb.2023.123171
41. A.K. Haridas, J. Heo, X. Li, H.-J. Ahn, X. Zhao et al., A flexible and free-standing FeS/sulfurized polyacrylonitrile hybrid anode material for high-rate sodium-ion storage. Chem. Eng. J. **385**, 123453 (2020). https://doi.org/10.1016/j.cej.2019.123453
42. D. Zhao, Z. Chen, W. Yang, S. Liu, X. Zhang et al., MXene (Ti_3C_2) vacancy-confined single-atom catalyst for efficient functionalization of CO_2. J. Am. Chem. Soc. **141**(9), 4086–4093 (2019). https://doi.org/10.1021/jacs.8b13579
43. Y. Zhao, X. Jia, G. Chen, L. Shang, G.I.N. Waterhouse et al., Ultrafine NiO nanosheets stabilized by TiO_2 from monolayer NiTi-LDH precursors: an active water oxidation electrocatalyst. J. Am. Chem. Soc. **138**(20), 6517–6524 (2016). https://doi.org/10.1021/jacs.6b01606
44. J. Duan, S. Chen, C.A. Ortíz-Ledón, M. Jaroniec, S.-Z. Qiao, Phosphorus vacancies that boost electrocatalytic hydrogen evolution by two orders of magnitude. Angew. Chem. Int. Ed. **59**(21), 8181–8186 (2020). https://doi.org/10.1002/anie.201914967
45. J. Wang, Y. Liu, G. Yang, Y. Jiao, Y. Dong et al., MXene-Assisted NiFe sulfides for high-performance anion exchange membrane seawater electrolysis. Nat. Commun. **16**(1), 1319 (2025). https://doi.org/10.1038/s41467-025-56639-7
46. F. Fungura, W.R. Lindemann, J. Shinar, R. Shinar, Carbon dangling bonds in photodegraded polymer: fullerene solar cells. Adv. Energy Mater. **7**(6), 1601420 (2017). https://doi.org/10.1002/aenm.201601420
47. Y. He, L. Ding, X. Wu, Q. Li, Z. Li et al., Hydrogen release mechanisms of MgH_2 over NiN4-embedded graphene nanosheet: First-principles calculations. Int. J. Hydrog. Energy **47**(93), 39549–39562 (2022). https://doi.org/10.1016/j.ijhydene.2022.09.102
48. D. Chen, R. Lu, R. Yu, Y. Dai, H. Zhao et al., Work-function-induced interfacial built-in electric fields in Os-$OsSe_2$ heterostructures for active acidic and alkaline hydrogen evolution. Angew. Chem. Int. Ed. **61**(36), e202208642 (2022). https://doi.org/10.1002/anie.202208642
49. P. Kuang, Z. Ni, B. Zhu, Y. Lin, J. Yu, Modulating the d-band center enables ultrafine Pt_3Fe alloy nanoparticles for pH-universal hydrogen evolution reaction. Adv. Mater. **35**(41), 2303030 (2023). https://doi.org/10.1002/adma.202303030
50. H. Wu, J. Hao, Y. Jiang, Y. Jiao, J. Liu et al., Alkaline-based aqueous sodium-ion batteries for large-scale energy storage. Nat. Commun. **15**(1), 575 (2024). https://doi.org/10.1038/s41467-024-44855-6
51. Y. Fu, J. Sun, Y. Zhang, W. Qu, W. Wang et al., Revealing Na^+-coordination induced failure mechanism of metal sulfide anode for sodium ion batteries. Angew. Chem. Int. Ed. **63**(27), e202403463 (2024). https://doi.org/10.1002/anie.202403463
52. Y. Feng, L. Zhou, H. Ma, Z. Wu, Q. Zhao et al., Challenges and advances in wide-temperature rechargeable lithium batteries. Energy Environ. Sci. **15**(5), 1711–1759 (2022). https://doi.org/10.1039/d1ee03292e
53. W. Zhao, S. Yuan, L. Zhang, F. Jiang, Y. Yang et al., Engineering metal-sulfides with cations-tunable metal-oxides electrocatalysts with promoted catalytic conversion for robust ions-storage capability. Energy Storage Mater. **45**, 1183–1200 (2022). https://doi.org/10.1016/j.ensm.2021.11.019
54. S. Zhao, G. Li, Z. Li, K. Zhang, X. Chen et al., Fast charging sodium-ion full cell operated from −50 ℃ to 90 ℃. Adv. Funct. Mater. **35**(1), 2411007 (2025). https://doi.org/10.1002/adfm.202411007
55. S. Qiao, Q. Zhou, M. Ma, H.K. Liu, S.X. Dou et al., Advanced anode materials for rechargeable sodium-ion batteries. ACS Nano **17**(12), 11220–11252 (2023). https://doi.org/10.1021/acsnano.3c02892
56. Y. Li, Q. Zhou, S. Weng, F. Ding, X. Qi et al., Interfacial engineering to achieve an energy density of over 200 Wh kg^{-1} in sodium batteries. Nat. Energy **7**(6), 511–519 (2022). https://doi.org/10.1038/s41560-022-01033-6
57. H. Lu, S. Chu, J. Tian, Q. Wang, C. Sheng et al., Ultra-high-energy density in layered sodium-ion battery cathodes through balancing lattice-oxygen activity and reversibility. Adv. Funct. Mater. **34**(2), 2305470 (2024). https://doi.org/10.1002/adfm.202305470
58. X. Shen, Q. Zhou, M. Han, X. Qi, B. Li et al., Rapid mechanochemical synthesis of polyanionic cathode with improved electrochemical performance for Na-ion batteries. Nat. Commun. **12**(1), 2848 (2021). https://doi.org/10.1038/s41467-021-23132-w
59. K. Zou, M. Jiang, T. Ning, L. Tan, J. Zheng et al., Thermodynamics-directed bulk/grain-boundary engineering for superior electrochemical durability of Ni-rich cathode. J. Energy Chem. **97**, 321–331 (2024). https://doi.org/10.1016/j.jechem.2024.05.053
60. P. Simon, Y. Gogotsi, B. Dunn, Materials science. Where do batteries end and supercapacitors begin? Science **343**(6176), 1210–1211 (2014). https://doi.org/10.1126/science.1249625

61. M.R. Lukatskaya, O. Mashtalir, C.E. Ren, Y. Dall'Agnese, P. Rozier et al., Cation intercalation and high volumetric capacitance of two-dimensional titanium carbide. Science **341**(6153), 1502–1505 (2013). https://doi.org/10.1126/science.1241488
62. K. Zheng, Y. Mu, M. Han, J. Liu, Z. Zou et al., Investigations of mechanisms leading to capacity differences in Li/Na/K-ion batteries with conversion-type transition-metal sulfides anodes. Adv. Sci. **11**(48), 2410653 (2024). https://doi.org/10.1002/advs.202410653
63. M. Han, J. Liu, C. Deng, J. Guo, Y. Mu et al., Yolk-shell structure and spin-polarized surface capacitance enable FeS stable and fast ion transport in sodium-ion batteries. Adv. Energy Mater. **14**(22), 2400246 (2024). https://doi.org/10.1002/aenm.202400246
64. M. Han, K. Zheng, J. Liu, Z. Zou, Y. Mu et al., Hollow microsphere structure and spin-polarized surface capacitance endow ultrafine Fe_7S_8 nanocrystals with excellent fast-charging capability in wide-temperature-range lithium-ion batteries. Adv. Energy Mater. **15**(12), 2403851 (2025). https://doi.org/10.1002/aenm.202403851
65. J. Zhu, S. Zhu, Z. Cui, Z. Li, S. Wu et al., Dual redox reaction sites for pseudocapacitance based on Ti and-P functional groups of $Ti_3C_2PBr_x$ MXene. Angew. Chem. Int. Ed. **63**(27), e202403508 (2024). https://doi.org/10.1002/anie.202403508
66. Q.-Q. Sun, T. Sun, J.-Y. Du, K. Li, H.-M. Xie et al., A sulfur heterocyclic quinone cathode towards high-rate and long-cycle aqueous Zn-organic batteries. Adv. Mater. **35**(22), 2301088 (2023). https://doi.org/10.1002/adma.202301088
67. X. Zhou, Y. Huang, B. Wen, Z. Yang, Z. Hao et al., Regulation of anion-Na^+ coordination chemistry in electrolyte solvates for low-temperature sodium-ion batteries. Proc. Natl. Acad. Sci. U.S.A. **121**(5), e2316914121 (2024). https://doi.org/10.1073/pnas.2316914121
68. Z. Yu, Q. Liu, D. Wang, J. Shi, D. Zhai et al., Unraveling electrode surface chemistry in determining interphase stability and deposition homogeneity for anode-free potassium metal batteries. Angew. Chem. Int. Ed. **64**(22), e202502091 (2025). https://doi.org/10.1002/anie.202502091
69. M.K. Aslam, I.D. Seymour, N. Katyal, S. Li, T. Yang et al., Metal chalcogenide hollow polar bipyramid prisms as efficient sulfur hosts for Na-S batteries. Nat. Commun. **11**(1), 5242 (2020). https://doi.org/10.1038/s41467-020-19078-0
70. X. Rui, D. Ren, X. Liu, X. Wang, K. Wang et al., Distinct thermal runaway mechanisms of sulfide-based all-solid-state batteries. Energy Environ. Sci. **16**(8), 3552–3563 (2023). https://doi.org/10.1039/d3ee00084b

 https://doi.org/10.1007/s40820-025-01858-2